Tribology International 210 (2025) 110752

Contents lists available at ScienceDirect

Tribology International

journal homepage: www.elsevier.com/locate/triboint

Full Length Article

Tire tread wear characteristics: Insights from indoor experiments and analytical modeling

Meng Zhang *, Hans-Joachim Unrau, Martin Gießler, Frank Gauterin

Institute of Vehicle System Technology, Karlsruhe Institute of Technology (KIT), Rintheimer Querallee 2, Karlsruhe, 76131, Germany

ARTICLE INFO

Keywords:
Tire tread wear characteristics
Analytical wear model
Indoor abrasion tests
Grosch wheel

ABSTRACT

This paper investigates tire tread wear characteristics across diverse operating conditions, where indoor tests and analytical modeling are employed. Experiments using Grosch wheels under controlled scenarios provide reliable data through four repetitions, with relative standard deviations mostly below 7.2%. The proposed model utilizes local friction states and a refined wear law to evaluate wear, achieving a root-mean-squared error ratio of 8.32%, which is one-third smaller than conventional wear models and can be further reduced by 5% when incorporating tread temperature. Finally, optimal vertical load and driving velocity conditions that minimize tread wear are analyzed based on the proposed model, providing a foundation for considering tire wear in vehicle driving strategies.

1. Introduction

A new passenger car tire loses 1~1.5 kg in weight over a service time of approximately 50 000 km [1]. Tire wear performance is an essential factor influencing both achievable mileage and environmental impact. Grigoratos et al. [2] reviewed multiple research and concluded that 0.1~10% by mass of worn rubber debris are emitted to the atmosphere as tire-road particle emissions, contributing to air pollution and impairing human respiration system. The use of electric vehicles (EVs) raises new challenges for tire abrasion. For instance, the weight of onboard batteries increases tire load, promoting the use of high inflation pressures to improve range (with lower tire rolling resistance), both of which affect tire wear performance.

Tire wear behavior is influenced by numerous factors, including tire type, inflation pressure, vertical load, driving style, and road surface properties [1,3]. Radial tires generally wear more slowly than bias tires [1,4]. Finite Element Analysis (FEA) simulations reveal that complex tread profiles contribute to 3.58 times faster tire wear compared to simple circumferential grooves [5]. Lowne [4] investigated the effect of road surface texture on tire wear performance, encountering a threefold increase in tire mass loss when switching from a smooth, polished surface to a rough, harsh one. Surface micro-texture emerged as the decisive reason while surface macro-texture played a moderating role. These findings are also supported by research [6,7]. However, there is a trade-off between reducing surface micro-texture and maintaining high tire grip, especially in wet conditions [8,9]. Interestingly, road surfaces become more abrasive after rain [6,10]. Specifically, one inch of accumulated rainfall increases the wear rate by 47% once the road surface dries again, which is attributed to the chemical surface etching effect of rainwater [6]. Furthermore, wet road surfaces are reported to cause less tire abrasion than dry ones [3,11], with a reduction in the wear rate of 30% on a harsh surface [6].

Tread temperature affects tire wear performance as well. Research [6,11,12] observed a positive relationship between rubber temperature and tire wear, with wear rate increasing by roughly 2% per degree Celsius [6]. However, some researchers encountered a negative correlation [13], while Yin [14] found a quadratic relationship where rubber abrasion first decreases and then increases with increasing temperature. Furthermore, winter tires used in summer experience faster wear as their tread rubber becomes softened [15], requiring larger slips to reach desired tire grips. However, using excessively hard tread compounds is not suggested due to the *magic triangle* conflict, in which enhancements in rolling resistance, wet grip, and abrasion resistance come at the expense of each other [16]. These properties are linked to the rubber's glass transition temperature: higher values typically lead to enhanced wet grip but lower abrasion resistance and higher rolling resistance [17,18]. An effective way to improve tire abrasion resistance while maintaining performance in the other two aspects is to modify the rubber compound, e.g., replacing carbon black with other rubber fillers like silica [19–21] and phosphonium-modified petroleum resin [16].

Compared to environmental factors, tire operating conditions such as driving velocity and vehicle acceleration play more important roles in tire wear performance [3]. Tire wear rate exhibits a positive correlation with driving velocities [13,22]. Research [6] found an exponential

* Corresponding author.
E-mail address: meng.zhang@kit.edu (M. Zhang).

https://doi.org/10.1016/j.triboint.2025.110752
Received 26 June 2024; Received in revised form 14 April 2025; Accepted 24 April 2025
Available online 13 May 2025

dependence of tire wear rate on tire friction force. The dependence of the wear rate on sideslip angle varies between second to fourth order according to different studies [11,13]. Additionally, the wear rate is approximately proportional to the third power of normal loads [13], though some studies note a near-linear increase with normal load [23,24]. Grosch [25] claims that the load dependency of tire wear is more influenced by tire contact length than a non-proportional relationship with vertical load. FEA simulations by Nguyen et al. [26] indicate that the wear rate is also affected by abrasion history and the frequency of reversing the tread rubber's sliding direction, yielding a peak wear rate at a typical frequency.

Other factors altering the contact status between the tire tread and the road surface also affect tire wear performance. Switching from 165/70 R14 to 175/70 R14 on the same vehicle increases tire lifespan by 20% due to a larger contact patch and lower contact pressure [3]. Similarly, lower inflation pressure results in a larger contact patch and reduced contact pressure. However, lower inflation pressures, although reducing wear rates observed in both bias and radial tires [27], have also been shown to increase wear rates in some simulations [28,29]. Notably, incorporating inflation pressure into tire modeling is challenging as inflation pressure not only influences tire footprint size but also alters the sidewall's stiffness [30]. Sakai [13] observed an optimal inflation pressure range of 2∼3 bar for minimal tire wear. Nonetheless, underinflated or overinflated pressure leads to uneven wear across the cross-section of tires, reducing the life span of a tire [27,31,32].

Tire wear is a cumulative process, and environmental disturbances during testing can influence final results. This variability partially explains the different results of the aforementioned research and, in turn, emphasizes the importance of exploring tire wear under controlled environments. Despite extensive efforts devoted to tire wear performance, tire tread wear characteristics across different operating conditions still lack reliable and interpretable clarification. On the other hand, modeling approaches afford another way to evaluate tire wear based on operating conditions, reducing the influences of experimental uncertainties. For example, Archard's wear law [33] provides a fundamental framework to assess frictional abrasion [34–36], and Schallamach's friction power-based wear law [37] further offers a simple way to evaluate the wear of rolling tires [5,26,28,29,38,39]. However, the straightforwardness of this kind of wear calculation approach compromises its accuracy under complex operating conditions, especially involving speed- and load-varying scenarios [40]. Improvements are still needed in model interpretability across diverse conditions and the inclusion of tire tread temperature. In addition, given the high time cost of abrasion tests, achieving high accuracy with limited calibration data also remains a practical challenge for tire wear models.

This paper investigates tire tread wear characteristics by integrating indoor tests and modeling approaches. Indoor tests using Grosch wheels are repeated four times for each scenario to provide reliable abrasion data under controlled operating conditions. Using brush theory, an analytical tread wear model is developed by integrating local friction states of tread rubber with an improved wear law based on frictional shear stress and local sliding velocity. The model exhibits high accuracy and good interpretability, with the capability to account for tread temperature for better performance. Finally, tire tread wear characteristics under various vertical loads and driving velocities are explored based on the proposed model. This paper is organized as follows: Section 2 introduces abrasion experiments carried out on an indoor test rig. Section 3 presents the details of the proposed analytical model. In Section 4, the performance of the proposed model is examined with experiments, and tire wear characteristics are investigated. Finally, Section 5 summarizes the valuable findings of this research and provides insights for future work.

Table 1
Technical parameters of the Grip and Abrasion Test Stand.

Items	Value	Unit
Track radius R_t	60	mm
Wheel radius	36	mm
Wheel width	18	mm
Rim radius	30	mm
Rotation speed	[0, 1000]	r/min
Sideslip angle	[0, 37.5]	°
Force F_x, F_y, F_z	[0, 200]	N

2. Experimental

2.1. Test bench preparation

The Grip and Abrasion Test Stand (GAT), developed at Karlsruhe Institute of Technology (KIT) [41], serves as the platform for wear experiments in this research. Similar to the LAT100 tire tread compound tester [40,42], GAT is a compact indoor test bench that has a closed chamber and a dedicated air circulation system, as shown in Fig. 1. An air conditioner is integrated into the air circulation system to keep the ambient temperature constant inside the chamber. GAT offers a variety of testing scenarios, including dry and wet grip, rubber specimens in block and Grosch wheel configurations, and different road surfaces such as realistic drilled road cores, sandpaper, safety walk, and carborundum disc.

In GAT, rubber specimens remain stationary while the abrasive road disc rotates under the motor drive. When using the Grosch wheel, the wheel is always in free-rolling and its steering angle (termed sideslip angle hereinafter) can be adjusted via a step motor. Both the disc's rotating speed and the wheel's sideslip angle are precisely controlled by a programmable management system. The vertical load of rubber specimens is regulated through a pneumatic system. Signals including rotation speed, sideslip angle, vertical load, rubber surface temperature, and the friction force of rubber specimens are recorded in real-time by the data acquisition system. In addition, a powder feeding device is available for abrasion tests, automatically adding powders to the track surface at a desired feed rate. Core functional parameters of GAT and Grosch wheel dimensions are listed in Table 1.

2.2. Test program

The wear performance of Grosch wheels under different vertical loads F_z, sideslip angles α, and driving velocities v_0 are of interest, forming three test groups. Each group includes two test cycles with three operating conditions. The test duration is determined to ensure an equal sliding distance in the lateral direction of Grosch wheels, as calculated by Eq. (1).

$$L_s = v_0 \cdot t \cdot \sin\alpha \tag{1}$$

where L_s denotes the lateral sliding distance and t is the test duration.

This study mainly accounts for the following two effects that affect the abrasion results of Grosch wheels.

- The road surface gets polished as abrasion tests progress, resulting in sequence dependency where initial test runs have a more abrasive surface than subsequent ones.
- The side force induces slight bending of the Grosch wheel, leading to adaptive uneven wear across its cross-section, with one shoulder more abrasion than the other.

To improve test reliability and repeatability, each operating condition is measured in an individual test run and has four repetitions. The test procedure is schematically shown in Fig. 2(a). Specifically, each test group consists of two test cycles in a reversed test sequence. Every test cycle includes two repetitions for each operating condition, and

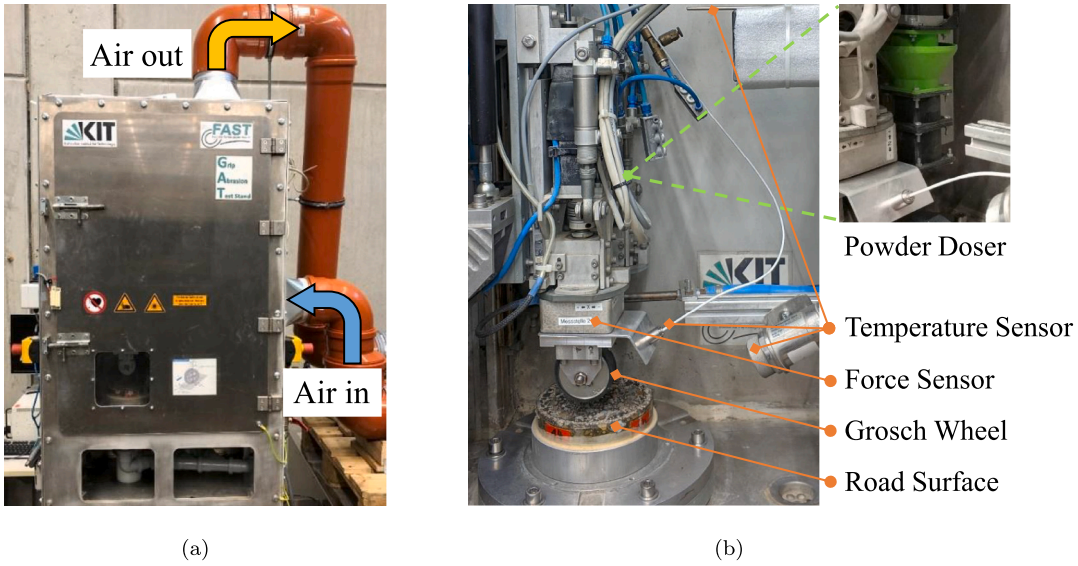

Fig. 1. Grip and Abrasion Test Stand: (a) front view; (b) internal view.

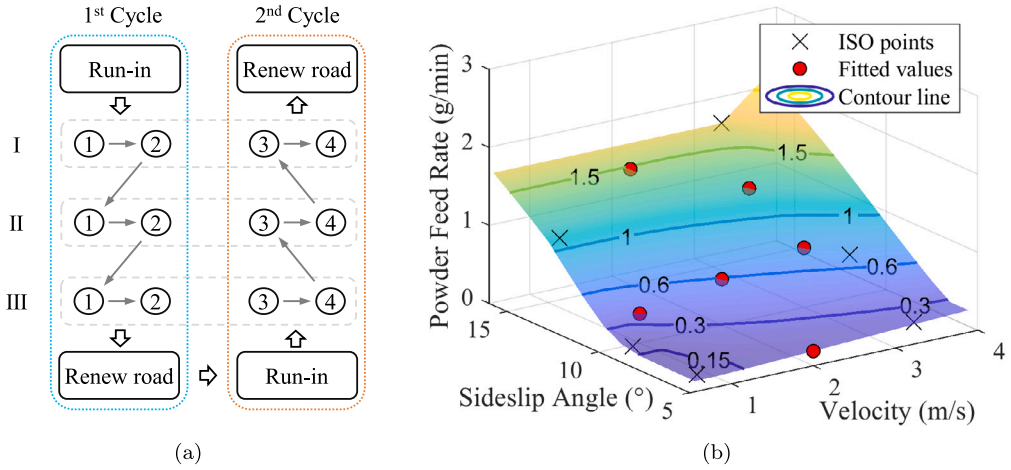

Fig. 2. Abrasion tests preparation. (a) Test sequence within a test group, where Roman numerals I, II, and III represent various operating conditions. Circled numbers denote different repetitions. (b) Interpolated powder feed rate under various sideslip angles and speeds based on ISO 23233 [43].

Table 2
Abrasion test program of Grosch wheels.

Conditions	v_0 (m/s)	α (°)	F_z (N)	Time (s)	Powder (g/min)
Run-in	3	13	75	150	1.112
Velocity	**1**	10	75	900	0.335
	2	10	75	450	0.627
	3	10	75	300	0.744
Sideslip Angle	2	**5**	75	897	0.166
	2	**10**	75	450	0.627
	2	**15**	75	303	1.471
Vertical Load	2	10	**50**	450	0.627
	2	10	**75**	450	0.627
	2	10	**100**	450	0.627

the mounting orientation of Grosch wheels is reversed after each test run (180° steering angle). Moreover, every test cycle starts with a new Grosch wheel and a run-in pre-treatment is utilized to remove the oxidized skin of the Grosch wheel. The road surface is renewed through sandblasting at the end of each test cycle.

GAT chamber maintained a constant ambient temperature of 23 °C during tests. Given that drilled road cores are not durable enough for the iterative sandblasting process, a carborundum disc was utilized. Anti-smearing powder[1] was used to avoid abraded rubber debris sticking on the road surface. The feed rate of powder was determined by referencing ISO 23233 [43], varying with the severity of operating conditions, as depicted in Fig. 2(b). The severity of operating conditions was determined based on the tread morphological behavior of Grosch wheels in trial tests (see Fig. 3(a)), aiming to avoid the smearing effect. The final test program is listed in Table 2.

2.3. Test results

An example of the real-time working condition data of Grosch wheels recorded during the test can be found in Fig. A.18 enclosed in Appendix. The wheels after abrasion tests are demonstrated in Fig. 3(a). The mass loss of Grosch wheels in each test run was measured with a precision of 1 mg. Notably, it was observed that the net weight of Grosch wheels increased overnight compared to their weight right after the abrasion tests, which might come from water absorption [45,46].

[1] Powder components: ISO 12103-1 [44].

Table 3
Summary of the mean measured side force and wear rate of Grosch wheels in the abrasion tests.

Conditions	v_0 (m/s)	α (°)	F_z (N)	F_y (N)	Average (g/km)	RSD (%)
Velocity	**1**	10	75	50.60	0.474	7.2
	2	10	75	50.48	0.659	6.2
	3	10	75	52.50	0.742	4.4
Sideslip Angle	2	**5**	75	21.79	0.199	15.2
	2	**10**	75	48.78	0.594	6.8
	2	**15**	75	62.59	1.374	2.2
Vertical Load	2	10	**50**	39.09	0.456	2.5
	2	10	**75**	49.30	0.608	3.1
	2	10	**100**	57.99	0.800	4.9
Benchmark	2	10	75	49.52	0.620	7.2

Therefore, it is necessary to ascertain the mass loss immediately after test runs. All abrasion results were converted into wear rate in mass loss per unit traveling distance by Eq. (2). To examine the impact of the test sequence on the results of abrasion tests, the wear rate of different test runs was normalized relative to the average wear rate of the benchmark scenario ($v_0 = 2$ m/s, $\alpha = 10°$, $F_z = 75$ N) in the same test group, as described in Eq. (3).

$$\hat{W}_r = \frac{\Delta m}{v_0 \cdot t} \tag{2}$$

$$\hat{W}_{r,norm} = \hat{W}_r / \bar{W}_{r,ref} \tag{3}$$

where Δm denotes the mass loss of Grosch wheels in each test run. $\bar{W}_{r,ref}$ refers to the average wear rate of the benchmark scenario.

Regression analysis was utilized to capture the trend of the wear rate across different conditions, with the fitting goodness indicated by the coefficient of determination (R^2), as depicted in Eq. (4). The normalized results $\hat{W}_{r,norm}$ for different test groups are demonstrated in Fig. 3(b), 3(c), and 3(d), respectively. The first cycle curves generally have a lower slope compared to the second cycle curves, supporting the presence of the polishing effect on the road surface. Moreover, the results indicate that the effects of vertical load, driving velocity and sideslip angle on the wear rate manifest in different patterns overall. Specifically, the wear rate demonstrates sub-linearly correlation with driving velocity, a super-linear correlation with sideslip angle, and a linear growth with vertical load.

$$R^2 = 1 - \frac{\sum_{i=1}^{N}(x_i - \hat{x}_i)^2}{\sum_{i=1}^{N}(x_i - \bar{x})^2} \tag{4}$$

$$r_{sd} = \sqrt{\frac{1}{N} \cdot \sum_{i=1}^{N}(x_i/\bar{x} - 1)^2} \times 100\% \tag{5}$$

where N is the number of tests included in the evaluation. x_i denotes measured data from the ith test. $\hat{x}_i$ represents the predicted value for the ith test. $\bar{x}$ refers to the average value of all measured data.

To quantitatively assess the repeatability of the abrasion tests, the relative standard deviation (RSD) of the wear rate was calculated for each operating condition as well as all the benchmark tests from different test groups, as depicted in Eq. (5). The results are listed in Table 3, in which the mean side force from the averages of four repetitions is also included. Additionally, the comparison between observed side force and those predicted by the model described later is enclosed in Appendix Fig. A.19 for reference. The deviation of the wear rate is mostly limited to less than 7.2%. The most visible deviation occurred in the mildest operating scenario ($v_0 = 2$ m/s, $\alpha = 5°$, $F_z = 75$ N), in which experimental uncertainties play a more significant role due to the low base wear rate. Since the RSD values for each operating condition and the benchmark tests from different groups remain relatively small, the abrasion tests with the proposed four repetitions in GAT are considered repeatable and reliable.

3. Modeling

Indoor test rigs have limitations in measuring wear performance under extreme operating conditions due to the smearing effect. Furthermore, the experiments alone cannot explain the wear behaviors observed. This section presents an analytical wear model by integrating a refined wear law using generalized friction power with tire local friction states investigated in a prior study [47], aiming to accurately assess tread wear performance.

3.1. Contact patch and friction law

A two-dimensional (2D) contact patch is employed to account for the speed difference between the inner and outer edges of Grosch wheels induced by the circular track of GAT. Given that the cross-section of Grosch wheels is flat, the footprint shape is assumed to be a rectangle. Contact width $2b$ remains constant irrespective of vertical load, while the relationship between contact length $2a$ and the vertical load F_z is ascertained using a regression model, as illustrated in Eq. (6).

$$a = a_1 \left(\frac{F_z}{1\,\mathrm{N}}\right)^{a_2} + a_3 \tag{6}$$

where a_1, a_2, and a_3 are regression parameters to be determined by measuring the footprint size of Grosch wheels under various vertical loads.

Taking the footprint center as the coordinate system origin (refer to Fig. 6), the contact pressure distribution across a 2D contact patch is developed in two steps.

- Establish a 1D contact pressure distribution, determining the line load density $f_z(x)$ along contact length using Eqs. (7) [48].
- For each circumferential position x, further distribute $f_z(x)$ in the transverse direction of the footprint using Eq. (8).

$$\begin{cases} f_z(x) = \dfrac{F_z}{2a} \cdot g_x\left(\dfrac{x}{a}\right) \\ g_x\left(\dfrac{x}{a}\right) = A_x\left(1 - \left(\dfrac{x}{a}\right)^{2n_x}\right)\left(1 + \lambda_x\left(\dfrac{x}{a}\right)^{2n_x}\right)\left(1 - B_x \cdot \dfrac{x}{a}\right) \\ A_x = \dfrac{(2n_x+1)(4n_x+1)}{2n_x(4n_x+1+\lambda_x)} \\ B_x = -\dfrac{3(2n_x+3)(4n_x+3)(4n_x+1+\lambda_x)}{(2n_x+1)(4n_x+1)(4n_x+3+3\lambda_x)} \cdot \dfrac{x_e}{a} \end{cases} \tag{7}$$

$$p(x,y) = \frac{f_z(x)}{2b} \cdot g_y\left(\frac{y}{b}\right) \tag{8}$$

where parameters n_x, λ_x and x_e regulate the load distribution pattern of g_x. Analogous to g_x, the function g_y governs the distribution pattern of contact pressure in the transverse direction, with a separate set of parameters n_y, λ_y and y_e. The resulting 2D pressure distribution satisfies the constraints shown in Eqs. (9).

$$\begin{cases} \int_{-a}^{a}\int_{-b}^{b} p(x,y)\,\mathrm{d}y\mathrm{d}x = F_z \\ \int_{-a}^{a}\int_{-b}^{b} p(x,y)x\,\mathrm{d}y\mathrm{d}x = F_z x_e \\ \int_{-a}^{a}\int_{-b}^{b} p(x,y)y\,\mathrm{d}y\mathrm{d}x = F_z y_e \end{cases} \tag{9}$$

A speed-dependent friction law, the Savkoor friction law [49], is used to describe the coefficient of friction (CoF) between tread rubber and the road surface under different sliding velocities, as demonstrated in Fig. 4. Since the raw Savkoor friction law neglects contact pressure, a pressure-dependent factor $sat(p)$ is incorporated to further improve its accuracy under different contact pressures, as depicted in Eqs. (10) and (11).

$$\mu = sat(p) \cdot \overbrace{\left(\mu_0 + (\mu_m - \mu_0) \cdot exp\left(-h^2 log_{10}^2\left(\frac{v_s}{v_m}\right)\right)\right)}^{\mu_s} \tag{10}$$

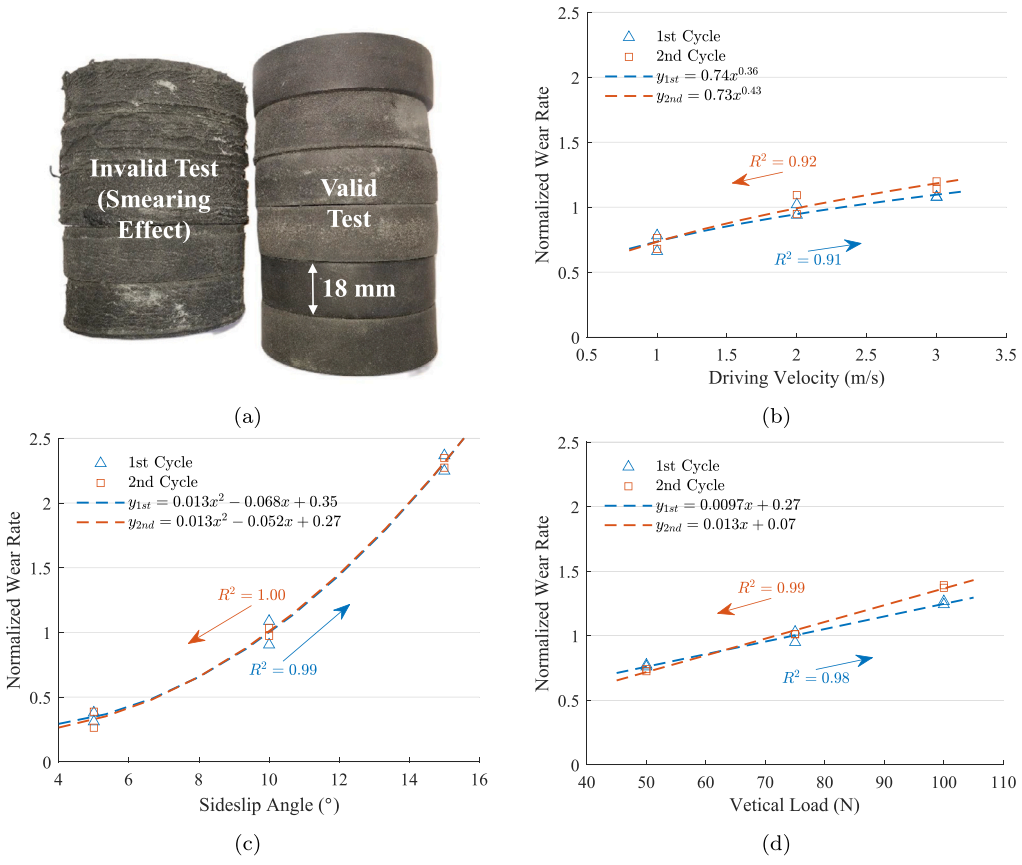

Fig. 3. Abrasion results: (a) invalid (left) and valid (right) tests; (b)~(d) normalized abrasion results under various driving velocities, sideslip angles, and vertical loads, respectively. Arrows indicate the test sequence within the test cycle.

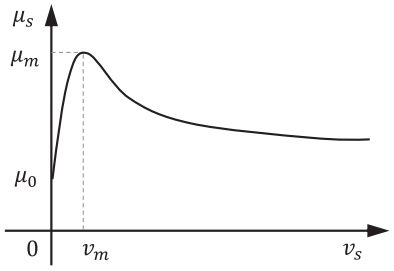

Fig. 4. Savkoor friction law: μ_0 and μ_m refer to the static and maximum attainable CoF, respectively. v_s represents the sliding velocity. v_m indicates the sliding velocity at which μ_m is reached. When $v_s < v_m$, a greater v_s deduces a larger CoF. Conversely, when $v_s > v_m$, the CoF declines as v_s increases. h regulates the varying rate of CoF with v_s.

$$sat(p) = \begin{cases} (p_0/p_{ref})^{-q} & \text{if} \quad p < p_0 \\ (p/p_{ref})^{-q} & \text{if} \quad p \geq p_0 \end{cases} \tag{11}$$

where p denotes the local contact pressure derived from Eq. (8). Additionally, p is set to a threshold value p_0 in $sat(p)$ when $p < p_0$, thereby avoiding unrealistic CoF at low contact pressure. p_{ref} represents a reference contact pressure. q denotes the varying rate of CoF with contact pressure.

3.2. Local friction states

The brush theory is utilized to analyze the detailed friction states of tread rubber. This theory categorizes the contact between the tire tread and the road surface into sticking and sliding states, depending on the relationship between frictional shear stress and attainable friction, as schematically shown in Fig. 5(a). Conventional brush models neglect the viscoelasticity and inertia of tread rubber, which limits their ability to capture the dynamic frictional responses of rubber compounds [50]. This study addresses this limitation by adopting massed Kelvin–Voigt elements, as depicted in Fig. 5(b). The modified element incorporates damping and inertia in addition to the stiffness of tread rubber, enabling a more realistic representation of the dynamic force response of tread rubber, as described in Eq. (12).

$$\tau = \underbrace{k\,\delta}_{\tau_k} + \underbrace{c\,\frac{\mathrm{d}\,\delta}{\mathrm{d}\,t}}_{\tau_c} + \underbrace{m\,\frac{\mathrm{d}^2\,\delta}{\mathrm{d}\,t^2}}_{\tau_m} \tag{12}$$

where τ_k, τ_c, and τ_m refer to the force responses from the spring, damping and inertia components, respectively.

The stiffnesses in the circumferential and transverse directions of the tire tread are denoted by k_x and k_y, and the damping coefficients are denoted by c_x and c_y, respectively. In addition, k_x and k_y are adaptable to the vertical load F_z, as expressed in Eqs. (13).

$$\begin{cases} k_y = k_{y0} + k_{y1}\,F_z \\ k_x = \varphi\,k_y \end{cases} \tag{13}$$

where φ indicates the anisotropy of tread rubber. k_{y0} and k_{y1} denote the influence of vertical load on the stiffness of tread rubber.

The Grosch wheel follows a circular track in GAT, and the deflection process of its tread rubber is shown schematically in Fig. 6. The tread elements on the inner edge of the contact patch experience traction, while those on the outer edge undergo braking. At a specified position (x, y) within the contact patch, the relative circumferential and transverse velocities between the associated tread element and the road surface are obtained based on Eqs. (14).

$$\begin{cases} v_{rx} = -\omega_z(y + \delta_y) \\ v_{ry} = -\omega_z R_t \sin\alpha + \omega_z(x + \delta_x) \end{cases} \tag{14}$$

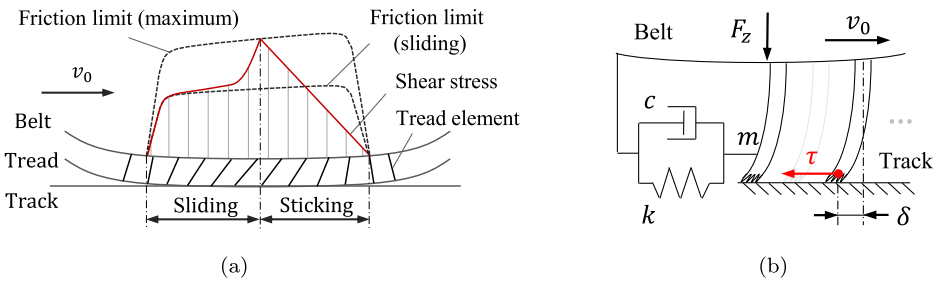

Fig. 5. Tire tread friction based on the brush theory. (a) Tread contact status and the associated frictional shear stress in braking. (b) Massed Kelvin–Voigt element. δ represents the tangential deflection of tread elements, and τ is the resulting frictional shear stress. The parameters k, c and m denote the equivalent stiffness, damping coefficient, and inertia of tread rubber per unit contact area, respectively.

where δ_x and δ_y represent the circumferential and transverse deflections of the tread element, respectively. The values of δ_x and δ_y are calculated as the integrals of the deflecting velocities of the tread element from the leading edge to the specified position (x, y), as shown in Eqs. (15).

$$\begin{cases} \delta_x = -\int_a^x \dfrac{v_{dx}}{v_0 \cos\alpha}\,\mathrm{d}x \\ \delta_y = -\int_a^x \dfrac{v_{dy}}{v_0 \cos\alpha}\,\mathrm{d}x \end{cases} \tag{15}$$

where v_{dx} and v_{dy} refer to the circumferential and transverse deflecting velocities of the tread element, respectively, with the minus sign indicating the directionality of the integral. The determination of v_{dx} and v_{dy} depends on the contact states of the tread element.

- $\tau < sat(p) \cdot \mu_0 p \rightarrow$ sticking case: $v_{dx} = v_{rx}$ and $v_{dy} = v_{ry}$.
- $\tau \geq sat(p) \cdot \mu_0 p \rightarrow$ sliding case: the relative sliding between the tread element and the road surface needs to be eliminated from v_{rx} and v_{ry}, as demonstrated in Eqs. (16).

$$\begin{cases} v_{dx} = v_{rx} + v_{sx} \\ v_{dy} = v_{ry} + v_{sy} \end{cases} \tag{16}$$

where $v_{sx} = v_s \cos\theta$ and $v_{sy} = v_s \sin\theta$ denote the longitudinal and lateral sliding velocities, respectively. Since friction force is speed-dependent, for any tread element in sliding, v_s and θ converge to values where the resulting frictional shear stresses can sustain the element's movement. This forms a force equilibrium regulated by a pair of ordinary differential equations (ODEs), as depicted in Eqs. (17) and (18). It is worth noting that in the sticking case, the frictional shear stress is obtained explicitly using Eqs. (17) as $v_s = 0$. Then, the global tread friction force is determined by integrating the shear stress across the entire contact patch.

$$\begin{cases} \dfrac{\mathrm{d}^2\delta_x}{\mathrm{d}t^2} = \dfrac{1}{m}\left(\tau_x - k_x\delta_x - c_x\dfrac{\mathrm{d}\delta_x}{\mathrm{d}t}\right) \\ \dfrac{\mathrm{d}^2\delta_y}{\mathrm{d}t^2} = \dfrac{1}{m}\left(\tau_y - k_y\delta_y - c_y\dfrac{\mathrm{d}\delta_y}{\mathrm{d}t}\right) \end{cases} \tag{17}$$

$$\begin{cases} \tau_x = \mu p \cos(\pi - \theta) \\ \tau_y = \mu p \sin(\pi - \theta) \end{cases} \tag{18}$$

where τ_x and τ_y represent the circumferential and transverse shear stresses acting on the tread element, respectively. The total frictional shear stress of the tread element τ equals $\sqrt{\tau_x^2 + \tau_y^2}$.

3.3. Wear law and model calibration

While the Schallamach's friction power-based method provides a general approach to calculating tire wear, its simplicity comes with limitations.

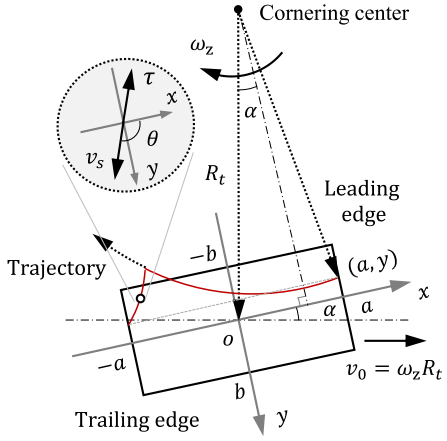

Fig. 6. The deforming status of tread rubber within the contact patch (top view). ω_z denotes the angular velocity of the road disc (clockwise is positive). v_s is the sliding velocity and θ represents the orientation angle of v_s.

- The method implicitly assumes equal contributions of friction force and relative velocity to wear. However, this assumption appears inconsistent with the experimental wear patterns revealed in Fig. 3. Additionally, research [13,40] also shows that considering friction force and velocity separately in the calculation matches better with observations.
- The approach focuses solely on abrasive wear resulting from sliding, while other mass removal mechanisms not fully captured by friction power are neglected, such as adhesive wear [51,52], and the variation in tread rubber indentation depth due to changes in contact pressure on road asperities [53].

To improve the wear evaluation, the conventional approach is modified by incorporating generalized friction power and an additional supplementary factor. The local wear rate of tread rubber (per unit contact area), denoted by w_r, is derived based on the local friction states obtained from Section 3.2. The global wear rate of the tire tread, denoted by W_r, is then determined by integrating the local wear rate across the contact patch. The calculation for w_r and W_r are expressed in Eqs. (19) and (20), respectively.

$$w_r = \left(w_4 + w_3 \overbrace{\left(\frac{\tau}{1\,\mathrm{MPa}}\right)^{w_1}\left(\frac{v_s}{1\,\mathrm{m/s}}\right)^{w_2}}^{\text{generalized friction power}}\right) \cdot \frac{1}{v_0} \tag{19}$$

$$W_r = \int_{-a}^{a}\int_{-b}^{b} w_r\,\mathrm{d}y\mathrm{d}x \tag{20}$$

where w_1 and w_2 indicate the sensitivity of the local wear rate w_r to frictional shear stress and sliding velocity, respectively. w_3 represents the abrasion resistance of the tread rubber to abrasive wear. w_4 is the supplementary factor accounting for the default wear incurred by the

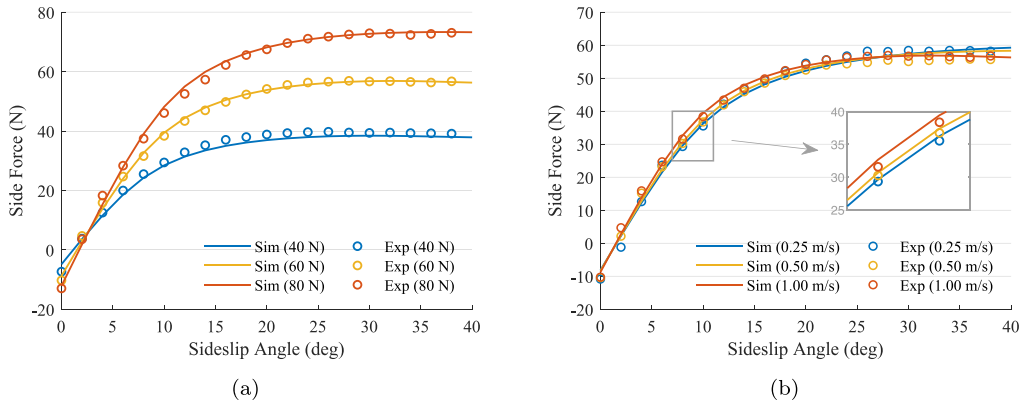

Fig. 7. Comparison of the side force between the proposed model and experiments. Notably, side force sign, relative to the coordinate system shown in Fig. 6, is reversed for better presentation. (a) Load varying condition with operating scenario (R_l = 60 mm, v_0 = 1 m/s), RMSE= 1.27 N. (b) Speed varying condition with operating scenario (R_l = 60 mm, F_z = 60 N), RMSE= 1.41 N.

Table 4
Identified model parameters related to the footprint, friction, and wear performance.

Footprint & Wear			Friction		
Item	Value	Unit	Item	Value	Unit
a_1	0.05	mm	μ_0	0.46	–
a_2	0.82	–	μ_m	1.15	–
a_3	1.37	mm	v_m	70.09	mm/s
b	9	mm	h	0.42	–
n_x	2.06	–	p_0	0.02	MPa
λ_x	0.52	–	p_{ref}	0.30	MPa
x_e	0.08	mm	q	0.14	–
n_y	4	–	φ	0.43	–
λ_y	1.84	–	k_{y0}	0.92	MPa/mm
y_e	0	mm	c_x	1.16×10^{-4}	MPa/(mm/s)
w_1	0.31	–	c_y	5.60×10^{-4}	MPa/(mm/s)
w_2	2.20	–	m	2.00×10^{-8}	MPa/(mm/s^2)
w_3	0.13	mg/s	k_{y1}	5.42×10^{-3}	1/mm^3
w_4	5.38×10^{-4}	mg/s			

mechanisms listed in the second limitation above, which are beyond the scope of the obtained local friction states.

The proposed model involves three types of parameters to be identified, including footprint-related, friction-related, and wear-related (see Table 4). Accordingly, the following measurements were performed:

- Footprint-related: the footprint size of the Grosch wheel was measured using ink to determine the relationship between contact length and vertical load. The distribution pattern of contact pressure was determined using pressure-sensitive membranes.[2]
- Friction-related: the side forces of the Grosch wheel were measured under different sideslip angles, considering various vertical load and driving velocity conditions.
- Wear-related: abrasion experiments as demonstrated in Section 2.2.

The parameters were tuned using the least-squares method to minimize the root-mean-squared error (RMSE) between the observed data and the model predictions, as illustrated in Eq. (21). The identified parameters are listed in Table 4. The resulting comparison between the predicted and measured side forces of the Grosch wheel is provided in Fig. 7.

$$f_{min}: min(\text{RMSE}), \quad \text{RMSE} = \sqrt{\frac{1}{N}\cdot\sum_{i=1}^{N}(\hat{x}_i - x_i)^2} \tag{21}$$

where x_i and $\hat{x}_i$ are measured and predicted values, respectively. N denotes the number of observations.

[2] Fujifilm Prescale.

4. Results and discussion

This section first gives insight into the local friction states of tread rubber within the contact patch. Then, the model performance in assessing tread wear is validated through experiments. Finally, the wear characteristics of tread rubber throughout a variety of vertical load and driving velocity conditions are explored.

Notably, although the static friction limit $sat(p)\cdot\mu_0 p$ was utilized to identify the sticking and sliding states of tread elements in Section 3.2, hereinafter, it is only considered sliding when the shear stress τ exceeds $sat(p)\cdot\mu_m p$, i.e., when $v_s > v_m$. This classification is reasonable and helps to streamline the following discussion. Because v_m is typically small, the resulting wear is limited even with some sliding. In addition, a higher sliding velocity leads to a greater CoF when $v_s < v_m$, which inhibits a significant increase in v_s and maintains a relatively stable w_r.

4.1. Dynamic states on contact patch

Fig. 8 exemplifies the local sliding velocity distribution of tread elements across the contact patch. The sliding velocity v_s remains nearly steady on a very low level within the sticking zone, while in the sliding zone, v_s increases rapidly due to two mechanisms. First, the kinetic CoF decreases as v_s increases. Consequently, the resulting friction force becomes insufficient to sustain the deflection of tread elements, which initiates the recovery of tread elements. This recovery process in turn enlarges the relative sliding between tread elements and the road surface, further reducing the kinetic CoF. Second, the contact pressure diminishes as tread elements approach the trailing edge. This reduction further decreases the available friction force of tread elements and accelerates the increase in v_s.

Fig. 9 illustrates the shear stress distribution corresponding to Fig. 8. At the leading edge, the frictional shear stress experiences a sharp increase due to the inertia and viscoelastic effects. For the same reasons, the elastic part of the longitudinal shear stress τ_x, namely $\tau_{x,k}$, continues to increase slightly after entering the sliding zone. This increase persists until the associated deforming velocity v_{dx} reaches zero, where the $v_{sx,sl}$ curve intersects with the $-v_{rx}$ curve in Fig. 8(b). This behavior also occurs in the lateral direction. In addition, the hysteresis phenomenon is observed at the trailing edge, showing a residual elastic force when tread elements detach from the road surface.

Fig. 10 demonstrates the local wear rate distribution on the contact patch. The local wear rate w_r remains very small in the sticking zone but increases rapidly after entering the sliding zone. Moreover, since the circular track of GAT induces additional turn-slip on the contact patch, the tread has a higher local wear rate in its shoulder regions compared to its center line. This abrasion severity difference is assessed by using the mean wear rate along the contact length for a specified

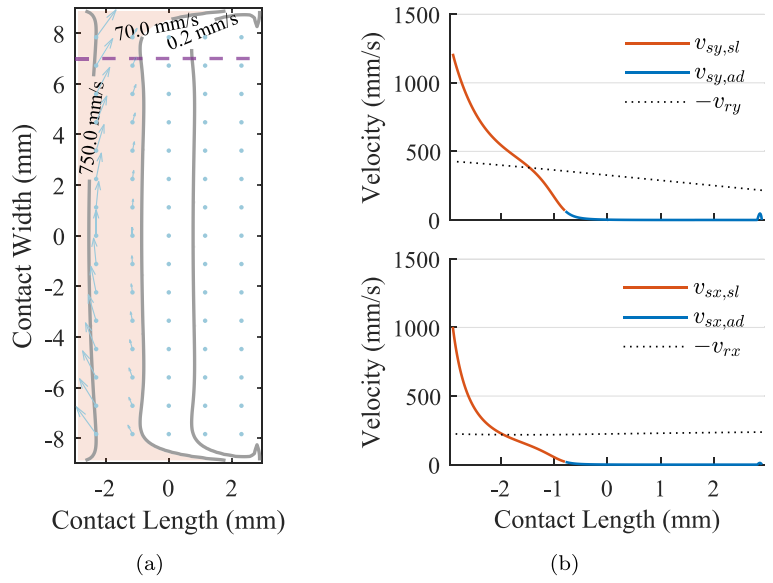

Fig. 8. Local sliding velocity distribution on the contact patch for the scenario ($v_0 = 2$ m/s, $\alpha = 10°$, $F_z = 75$ N). Leading edge: right side. (a) Brown area: the sliding zone. Light blue arrows: sliding velocity vectors. Gray contour lines: magnitude of v_s. (b) The upper and lower diagrams demonstrate v_{sy} and v_{sx} distributions along the contact length at the lateral position $y = 7$ mm, respectively. In each diagram, blue and brownish-red solid lines represent the corresponding sliding velocity in the sticking (ad) and sliding (sl) zones, respectively; dotted line derives from Eqs. (14).

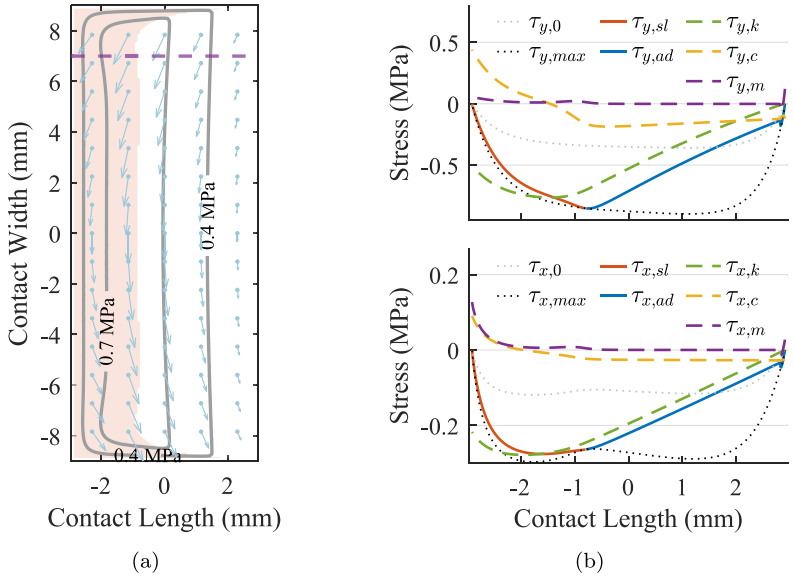

Fig. 9. Shear stress distribution on the contact patch for the scenario ($v_0 = 2$ m/s, $\alpha = 10°$, $F_z = 75$ N). Leading edge: right side. (a) Brown area: the sliding zone. Light blue arrows: shear stress vectors. Gray contour lines: magnitude of τ. (b) The upper and lower diagrams show τ_y and τ_x distributions along the contact length at the lateral position $y = 7$ mm, respectively. In each diagram, blue and brownish-red solid lines represent the related shear stress in sticking (ad) and sliding (sl) zones, respectively. Dashed lines indicate the three types of force responses derived from Eq. (12). Dotted lines refer to the friction limits, where $[\tau_{y,0},\ \tau_{x,0};\ \tau_{y,max},\ \tau_{x,max}] = sat(p) \cdot p \cdot [\mu_0;\ \mu_m] \cdot [\sin\theta,\ \cos\theta]$.

lateral position y, as defined in Eq. (22). The local wear rate distribution along the contact length and the mean wear rate distribution across the cross-section of the tread are depicted in Fig. 10(b).

$$\bar{w}_{r,y} = \frac{1}{2a}\int_{-a}^{a} w_r \mathrm{d}x \tag{22}$$

4.2. Experimental validation

The vertical load of the Grosch wheel fluctuates slightly in the abrasion tests as depicted in Fig. A.18. To reflect the realistic operating condition of the Grosch wheel, the recorded vertical load is employed as the input for the proposed model, rather than the pre-defined load in the abrasion procedure. Specifically, the recorded data from each test run are discretized into different bins regarding vertical load, with a bin width of 10 N. Then, the wear rate of the test run is eventually ascertained by calculating the weighted average wear rate of all bins, as described in Eq. (23).

$$W_r = \sum_{i=1}^{j} \beta_i \cdot W_{r,i} \tag{23}$$

where j is the number of bins derived from each test run. β_i denotes the proportion of data size for the ith bin in the test run. $W_{r,i}$ refers to the global wear rate calculated by the proposed model for the ith bin.

The root-mean-squared error ratio (RMSER), as defined by Eqs. (24), is utilized to evaluate the model's accuracy relative to observations. Fig. 11 demonstrates the comparison between the model results and

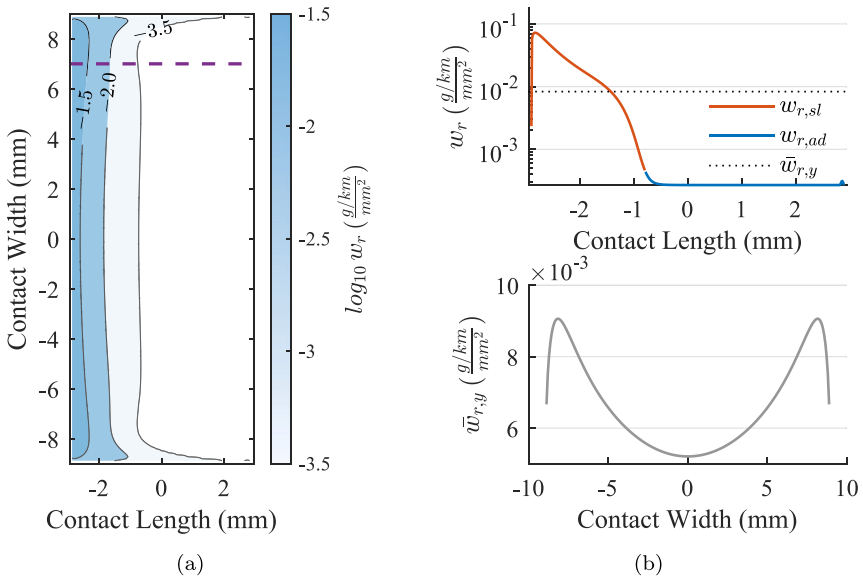

Fig. 10. Local wear rate distribution on the contact patch for the scenario (v_0 = 2 m/s, α = 10°, F_z = 75 N). Leading edge: right side. (a) Contour lines: magnitude of w_r in logarithmic scale. (b) The upper diagram: w_r distribution along the contact length at the lateral position y = 7 mm. Curves $w_{r,ad}$ and $w_{r,sl}$ represent local wear rate in the sticking (ad) and sliding (sl) zones, respectively. The lower diagram: $\bar{w}_{r,y}$ distribution along the cross-section of the tread.

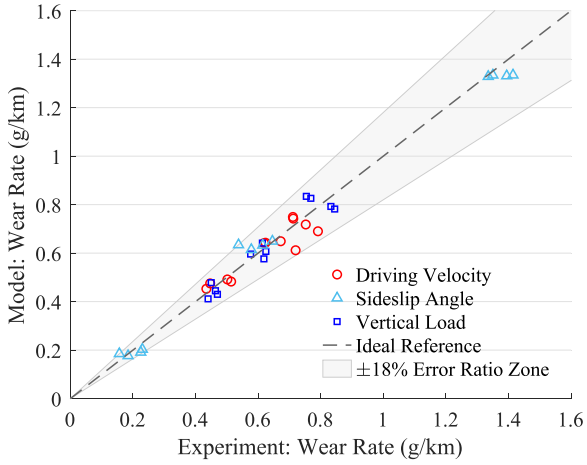

Fig. 11. Comparison of the global wear rate between the proposed model and experiments. Associated RMSER value: 8.32%.

the associated observations. The proposed model achieves an RMSER value of 8.32%, with a maximum error ratio of approximately 18%.

$$\begin{cases} y_{er,i} = \hat{x}_i / x_i - 1 \\ \text{RMSER} = \sqrt{\dfrac{1}{N} \cdot \sum_{i=1}^{N} y_{er,i}^2} \end{cases} \tag{24}$$

where $y_{er,i}$ is the error ratio of model results relative to observations. x_i, $\hat{x}_i$, and N remain the same meanings as in Eq. (21).

Studies [14,54,55] report that rubber wear rate initially decreases and then increases with increasing rubber temperature. To account for this temperature effect, the wear resistance factor w_3 in Eq. (19) is assumed to normally correlate with tread temperature within the measured temperature range, as illustrated in Eq. (25). The proposed wear model is termed as *Opt* and Opt_T before and after considering the tread temperature, respectively. The results of the model Opt_T are depicted in Fig. 12(a). Although the maximum error ratio remains at 18%, the RMSER value of model Opt_T is improved by approximately 5% compared to the model *Opt*. Specifically, the improvement mainly derives from the large sideslip angle condition (α = 15°), at which the tread temperature is relatively high.

$$w_3 \Rightarrow w_3 \cdot \exp\left(\frac{(T - T_0)^2}{2\sigma_T^2}\right) \tag{25}$$

where T is the average tread temperature of Grosch wheels in each test run, as shown in Fig. 12(b). T_0 represents a reference temperature at which tread rubber exhibits an optimal wear resistance. σ_T regulates the variation of rubber wear resistance regarding rubber temperature.

To provide a comparable reference, the performance of the conventional friction power-based approach using the measured tire force and the relative speed between the tire and the road surface is examined. Moreover, the conventional method is further enhanced with reference to the model *Opt*, as depicted in Eq. (26). Depending on the use of the generalized friction power and the inclusion of the temperature effect described in Eq. (25), four reference models are employed in the comparison. Specifically, they are defined as follows:

M_P : $w_1 = w_2$, without temperature effect.

M_{PT} : $w_1 = w_2$, with temperature effect.

M_{EP} : $w_1 \neq w_2$, without temperature effect.

M_{EPT} : $w_1 \neq w_2$, with temperature effect.

$$W_r = \left(w_4 + w_3\left(\frac{F_y}{1\,\text{N}}\right)^{w_1}\left(\frac{v_0 \sin\alpha}{1\,\text{m/s}}\right)^{w_2}\right) \cdot \frac{1}{v_0} \tag{26}$$

For these reference models, the recorded data are grouped into different bins based on side force, with a bin width of 10N. Then, the weighted wear rate is calculated using Eq. (23) for each test run. The parameters of the reference models are determined by minimizing the RMSE values between model results and observations. To better illustrate the accuracy difference among different models, the RMSER ratio of other models relative to the model *Opt* is utilized, denoted as *Error Ratio Index* (ERI). The results of the reference models and the model Opt_T are summarized in Table 5, revealing:

(1) Overall, the proposed models *Opt* and Opt_T have higher accuracy compared to these conventional models, with RMSER values one-third smaller.

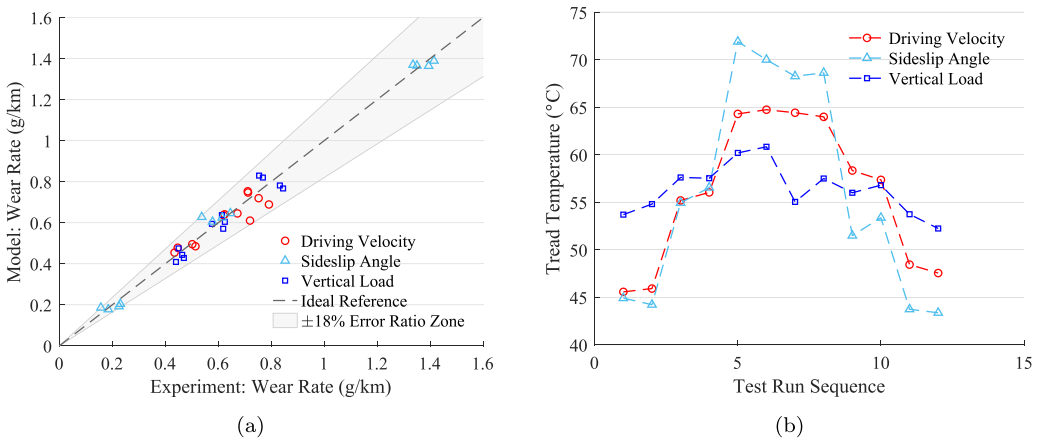

Fig. 12. Validation of the model Opt_T: (a) comparison of the global wear rate between the model Opt_T and experiments, with an RMSER value of 7.92%; (b) average tread temperature of Grosch wheels across abrasion tests (note: plotted with dashed lines only for visual clarity, not implying physical continuity).

Table 5
Model parameters and associated performance.

Model	w_1 –	w_2 –	w_3 10^{-2} (mg/s)	w_4 10^{-2} (mg/s)	T_0 (°C)	σ_T (°C)	RMSE 10^{-2} (g/km)	ERI –
M_P	1.36	1.36	2.32	9.53	–	–	6.09	1.87
M_{PT}	1.14	1.14	3.73	3.82	80.19	3.48	6.07	1.94
M_{EP}	1.11	1.48	7.22	0.11	–	–	5.74	1.59
M_{EPT}	0.90	1.27	6.56	5.71	145.36	−115.58	5.64	1.60
Opt	0.31	2.20	13.35	0.0538	–	–	4.38	1.00
Opt_T	0.31	2.28	13.25	0.0712	47.17	57.98	4.28	0.95

(2) The model Opt achieves a 5% reduction in the ERI value after considering the tread temperature. However, the models M_P and M_{EP} show little room to gain from this consideration. Although their temperature-adjusted counterparts M_{PT} and M_{EPT} achieve slightly smaller RMSE, this comes at the expense of decreased accuracy at mild operating conditions, as evidenced by increased ERI values.
(3) Using generalized friction power helps both models M_{EP} and M_{EPT} reach approximately 15% smaller ERI values relative to their original versions M_P and M_{PT}.

4.3. Wear characteristics

Based on the proposed model Opt, this section further explores tire tread wear characteristics across various vertical load and speed scenarios. Fig. 13(a) introduces the variation of the global wear rate of tread rubber W_r over side force under different vertical loads. This variation can be roughly divided into three stages regarding the rate of change.

- Initial plateau: When the sideslip angle is small, W_r varies modestly with increasing side force. The smaller the vertical load, the lower the global wear rate. Notably, W_r reaches its minimum value at a nonzero sideslip angle, which is attributed to the circular track.
- Steady growth: W_r then increases almost exponentially with side force. Moreover, the increase rate is greater for smaller vertical loads.
- Dramatic increase: When the side force approaches the tire's maximum grip, W_r increases dramatically as the sideslip angle continues to increase, even though the associated side force starts to decline.

After converting Fig. 13(a) into Fig. 13(b), it is clear that W_r exhibits a non-monotonic relationship with vertical loads for a constant side force, especially when this desired side force is at a moderate value. W_r initially decreases and then increases with rising vertical load, revealing the existence of an optimal vertical load for the desired side force. As adjusting inflation pressure can achieve a similar grounding area and contact pressure to varying vertical loads for pneumatic tires, this model results conform with the optimal inflation pressure observed in research [13] that yields the least tire wear. In addition, the non-monotonic relationship between W_r and vertical load is also in good agreement with observations on tire particulate matter (PM) emissions under different vertical loads [56], as depicted in Fig. 14. A lower vertical load is advantageous when the required tire force is small, whereas a higher vertical load is preferable when the required tire force is high. Although only a part of the tread wear is emitted as PM emissions, the tread wear severity indicated by both the abrasion and PM emission results is similar, e.g., more severe operating conditions correlate with higher PM emissions and more tread wear.

To clarify the occurrence of the optimal vertical load condition under a specified side force, the global wear rate W_r is assumed to change continuously and smoothly with increasing vertical loads F_z. Then, a vertical load condition yields the least global wear rate when Eqs. (27) holds.

$$\begin{cases} \dfrac{\partial W_r}{\partial F_z} = \dfrac{\partial A}{\partial F_z} \cdot \bar{w}_r + A \cdot \dfrac{\partial \bar{w}_r}{\partial F_z} \to 0 \\ \bar{w}_r = \left(w_4 + w_3 \cdot \left(\dfrac{\bar{\tau}}{1\,\mathrm{MPa}} \right)^{w_1} \left(\dfrac{\bar{v}_s}{1\,\mathrm{m/s}} \right)^{w_2} \right) \cdot \dfrac{1}{v_0} \sim \dfrac{W_r}{A} \end{cases} \tag{27}$$

where $A = 4ab$ is the area of the contact patch. $\bar{w}_r$ represents the average local wear rate on the contact patch. $\bar{\tau}$ and $\bar{v}_s$ refer to the equivalent average shear stress and sliding velocity of tread elements, respectively.

When the vertical load F_z increases, the contact area becomes bigger, making $\frac{\partial A}{\partial F_z}$ positive. Simultaneously, more tread elements come into contact with the road surface to transmit friction force, leading to reduced $\bar{\tau}$ and $\bar{v}_s$ for a specified tire force. As a result, $\frac{\partial \bar{w}_r}{\partial F_z}$ shows a negative value. Overall, the global wear rate increases with vertical loads if the effect of $\frac{\partial A}{\partial F_z} \cdot \bar{w}_r$ covers the effect of $A \cdot \frac{\partial \bar{w}_r}{\partial F_z}$. Otherwise, the

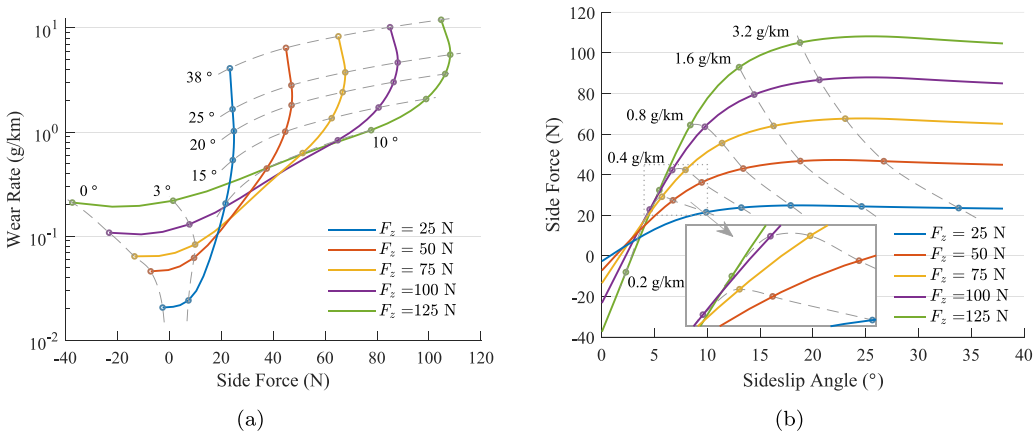

Fig. 13. Tread global wear rate under different vertical loads in the carpet plot. Operating condition: (R_t = 60 mm, v_0 = 2 m/s). The gray dashed lines represent the sideslip angle in (a) and the global wear rate in (b).

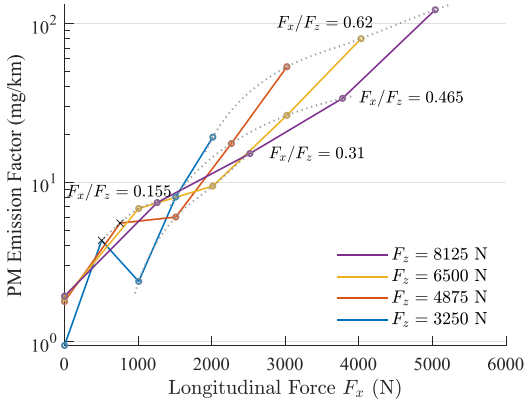

Fig. 14. PM emissions from full-size tires under specified tire grip utilization rates for different vertical loads. The marker "×" indicates data points deviating from expectations (Redrawn from the data in research [56]).

global wear rate declines with vertical loads. Since the local friction states of tread elements are governed by the nonlinear ODEs shown in Eqs. (17), analytically deriving the optimal vertical load to achieve the desired tire grip is challenging. This optimal condition is thus determined through numerical interpolation, as presented in Fig. 13.

Fig. 15(a) demonstrates the variation of the global wear rate with side force under different driving velocities. Since the sideslip angle rarely exceeds the value that generates maximum tire grip in realistic driving, for clarity, this study mainly focuses on scenarios before reaching the maximum tire grip. When the side force is small, higher driving velocities lead to a lower global wear rate W_r. However, as the driving velocity rises, W_r increases more rapidly with increasing side force. Consequently, higher driving velocities result in a larger W_r when the side force nears its peak.

For a specified side force, W_r exhibits a complicated relationship with driving velocity, as depicted in Fig. 15(b). When the side force is small, the resulting W_r consistently declines with increasing driving velocities. However, for larger side forces, the relationship between W_r and driving velocity consists of three phases. W_r initially decreases with increasing driving velocity, then increases, and finally decreases again at very high driving velocities. This relationship forms a local optimal driving velocity that yields the least wear, consistent with the observations on tire PM emissions across different driving velocities [56].

These complex behaviors are attributed to the different effects of driving velocity on tread wear in the sticking and sliding zones. To facilitate the subsequent discussion, the average local wear rate of tread rubber per unit time, $\bar{w}_{r,t}$, is introduced, calculated as $\bar{w}_{r,t} = \bar{w}_r \cdot v_0$.

- Sticking zone: The sliding velocity remains below the critical velocity of the friction law, v_m, yielding a low $\bar{w}_{r,t}$ near the offset wear rate (reflected by w_4 in Eq. (19)) regardless of driving velocity variations, as shown in Fig. 16(a).
- Sliding zone: $\bar{w}_{r,t}$ increases with increasing driving velocity until it reaches a plateau at high driving velocities.[3] The plateau appears due to the inertia effect of tread rubber, which restricts the maximum attainable sliding velocity within the contact duration.

On the other hand, increasing either the side force or the driving velocity results in a reduction in the area of the sticking zone [47]. Consequently, the eventual behaviors of the global wear rate W_r result from the interaction between the values of $\bar{w}_{r,t}$ in sticking and sliding zones and the corresponding areas of these two zones, as depicted in Fig. 16(b).

- When the sticking zone is the majority of the contact patch: the behavior of $\bar{w}_{r,t}$ in the sticking zone dominates W_r, yielding a declining W_r with increasing driving velocity.
- When the sliding zone is the majority of the contact patch: the behavior of $\bar{w}_{r,t}$ in the sliding zone dominates W_r. As a result, W_r shows an initial increase with driving velocity, and after $\bar{w}_{r,t}$ reaches its plateau, W_r decreases.

It is worth noting that W_r exhibits a local minimum value when the driving velocity satisfies the condition $v_0 \sin\alpha = v_m$, as demonstrated in Fig. 17. Interestingly, Persson et al. [55] performed a theoretical analysis and found that rubber compounds exhibit optimal wear performance near the temperature where the rubber reaches maximum friction. The optimal condition suggested by the proposed model conforms with their research, based on the temperature-velocity equivalence theory in rubber abrasion performance [54].

5. Conclusion

This paper characterized tire tread wear performance under different operating conditions by integrating indoor experiments with analytical modeling methods. Indoor abrasion tests were carried out on the Grip and Abrasion Test Stand using Grosch wheels. Test reproducibility was ensured by repeating each test run four times, with adjustments to test sequences, Grosch wheel installations, and road

[3] Tire temperature rise effect is not incorporated here.

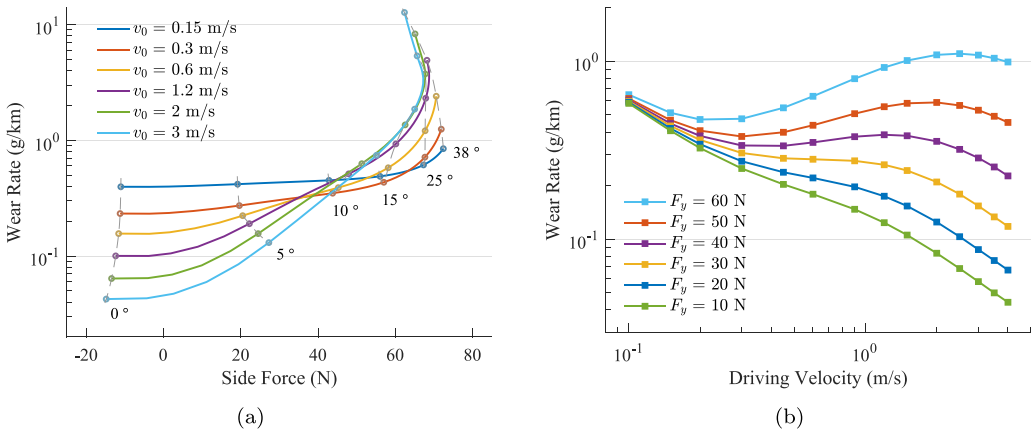

Fig. 15. Tread wear global wear rate under various driving velocities. Operating condition: (R_t = 60 mm, F_z = 75 N). (a) Tread global wear rate over side force for different driving velocities. The gray dashed lines represent the sideslip angle. (b) Tread global wear rate over driving velocity for different side forces.

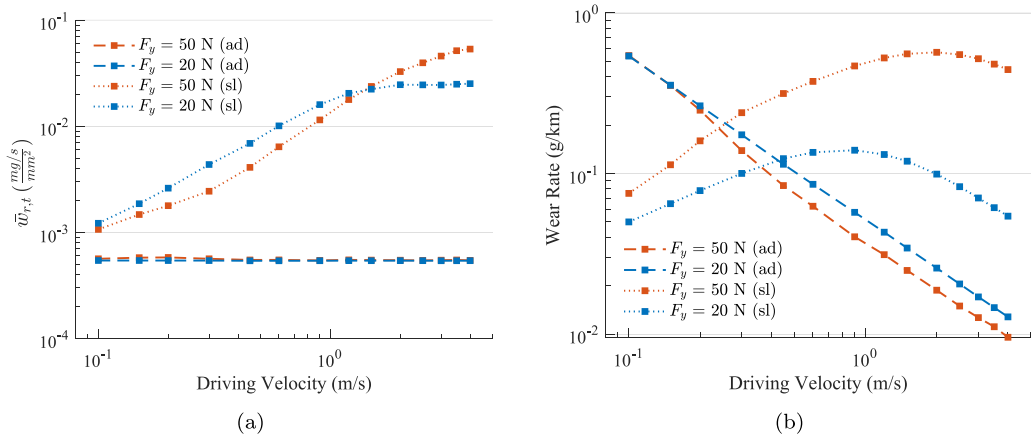

Fig. 16. Tread wear behaviors in the sticking (ad) and sliding (sl) zones under various driving velocities. Operating condition: (R_t = 60 mm, F_z = 75 N). (a) Tread average local wear rate per unit time. (b) Tread global wear rate per unit traveling distance.

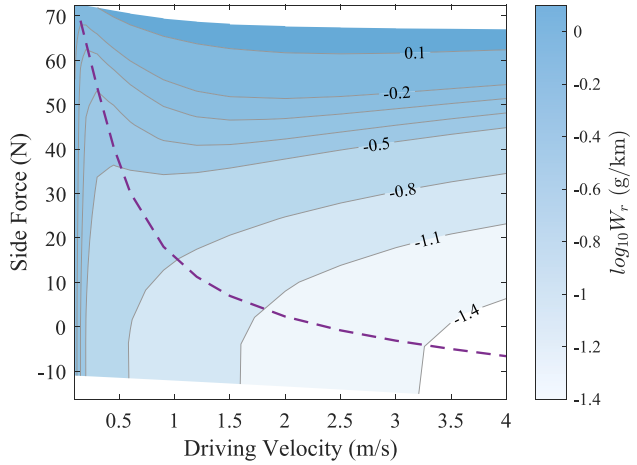

Fig. 17. Tread global wear rate under different side forces and driving velocities. Operating condition: (R_t = 60 mm, F_z = 75 N). The purple dashed line indicates the optimal side force (obtained at sideslip angle $\alpha = \arcsin(v_m/v_0)$) under various driving velocities.

surface sandblasting to mitigate polishing effects. Experimental results showed that the relative standard deviation across repetitions remained low, mostly below 7.2%, confirming the reliability of the testing procedure.

The proposed wear model was constructed based on brush theory and employed a modified wear law using generalized friction power. Local friction states of tread rubber were determined, accounting for viscoelasticity, inertia, and kinetic friction behaviors, and integrated with the refined wear law to evaluate tread wear. In comparison with experiments, the proposed model yielded a root-mean-squared error ratio (RMSER) of 8.32%, less than two-thirds of that from conventional wear models using global friction power. Moreover, the model exhibited potential to further reduce the RMSER value by approximately 5% when accounting for the tread temperature, whereas this refinement showed little improvement on the conventional models. Finally, analysis of tire wear characteristics across various driving velocities and vertical loads indicated that both of them had a non-monotonic relationship with the tread's global wear rate, revealing the existence of optimal vertical load and driving velocity conditions. These behaviors agree well with the observations from full-size tires and are effectively explained by the proposed model.

This study provides a valuable reference for obtaining reproducible abrasion tests on indoor test rigs and offers an analytical modeling method to evaluate tread wear performance, achieving high accuracy and good interpretability. The findings enhance understanding of tire tread wear behaviors and reveal a possible way to characterize tire-road particle emissions based on tire local friction states. Given that Grosch wheels work like a tiny tire and the local friction state-based analysis does not rely on hypotheses specific to Grosch wheels, the presented evaluation approach is also applicable to full-size tires. Future work will develop full-size tire models based on current modeling approach, in which flexible carcass compliance will be included.

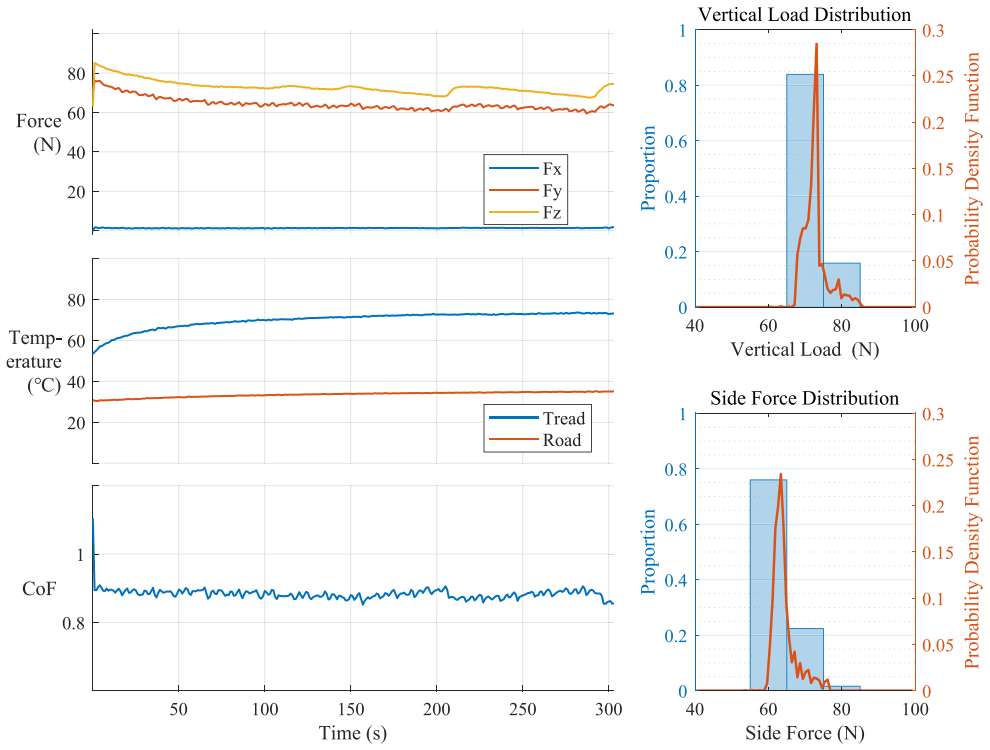

Fig. A.18. Real time working condition of the Grosch wheel recorded in abrasion tests. CoF denotes an abbreviation for coefficient of friction. Operating scenario: (v_0 = 2 m/s, α = 15°, F_z = 75 N). Sampling frequency: 50 Hz. Data smoothing method: moving average filter with a window width of 50.

CRediT authorship contribution statement

Meng Zhang: Writing – original draft, Visualization, Validation, Software, Methodology, Investigation, Formal analysis, Conceptualization. **Hans-Joachim Unrau:** Writing – review & editing, Supervision, Conceptualization. **Martin Gießler:** Writing – review & editing, Supervision. **Frank Gauterin:** Writing – review & editing, Supervision, Resources.

Declaration of competing interest

The authors declare the following financial interests/personal relationships which may be considered as potential competing interests: Meng Zhang reports financial support was provided by China Scholarship Council. If there are other authors, they declare that they have no known competing financial interests or personal relationships that could have appeared to influence the work reported in this paper.

Acknowledgments

The first author acknowledges support from the China Scholarship Council (CSC). We acknowledge support by the KIT-Publication Fund of the Karlsruhe Institute of Technology, Germany.

Appendix. Supplementary diagrams

See Figs. A.18 and A.19.

Data availability

Data will be made available on request.

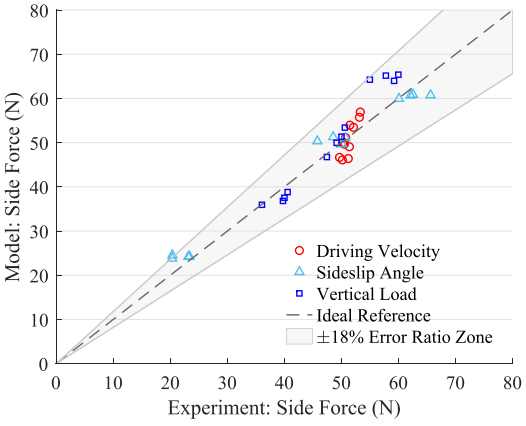

Fig. A.19. Comparison of side force between model predictions and observations in abrasion tests, with an RMSER value of 7.47%. Deviations primarily stem from two aspects: the model's friction performance was calibrated using separate friction measurements, not specific to abrasion tests; and the Grosch wheel's cross-sectional shape changes during testing, affecting wheel–road contact. Notably, experimental side force is represented by the average value throughout test runs, and the model prediction is calculated at the mean vertical load of associated test runs (other model inputs come from test conditions, such as driving speed and sideslip angle).

References

[1] Boulter P. A review of emission factors and models for road vehicle non-exhaust particulate matter. Transport Research Laboratory; 2005.
[2] Grigoratos T, Martini G. Non-exhaust traffic related emissions. brake and tire wear pm. Report EUR 26648, 2014.
[3] Le Maitre O, Süssner M, Zarak C. Evaluation of tire wear performance. Tech. rep. SAE Technical Paper, 1998.
[4] Lowne R. The effect of road surface texture on tire wear. Rubber Chem Technol 1971;44(5):1159–72.
[5] Li Z. Experimental and numerical study on tire tread wear behavior (Chinese) (Ph.D. thesis), University of Science and Technology of China; 2013.

[6] Veith AG. Accelerated tire wear under controlled conditions. II. Some factors that influence tire wear. Rubber Chem Technol 1973;46(4):821–42.
[7] Veith AG. Tire treadwear—the joint influence of compound properties and environmental factors. Tire Sci Technol 1995;23(4):212–37.
[8] Johannesson M, Lithner D. Potential policy instruments and measures against microplastics from tyre and road wear : mapping and prioritisation. VTI rapport 1092A, Swedish National Road and Transport Research Institute, Environment; 2022, https://urn.kb.se/resolve?urn=urn:nbn:se:vti:diva-18120.
[9] Gehrke I, Schläfle S, Bertling R, Öz M, Gregory K. Mitigation measures to reduce tire and road wear particles. Sci Total Environ 2023;166537.
[10] Lorenz B, Oh Y, Nam S, Jeon S, Persson B. Rubber friction on road surfaces: Experiment and theory for low sliding speeds. J Chem Phys 2015;142(19).
[11] Grosch K, Schallamach A. Tire wear at controlled slip. Wear 1961;4(5):356–71.
[12] Molnar W, Nevosad A, Rojacz H, Adam K, Henze H-J, Ripoll MR, et al. Two and three-body abrasion resistance of rubbers at elevated temperatures. Wear 2018;414:174–81.
[13] Sakai H. Friction and wear of tire tread rubber. Tire Sci Technol 1996;24(3):252–75.
[14] Yin H. Theoretical and experimental study on tire wear and temperature field (Chinese) (Ph.D. thesis), Qingdao University of Science & Technology; 2017.
[15] Sundt P, Syversen F, Skogesal O, Schulze P. Primary microplastic-pollution: Measures and reduction potentials in Norway. Mepex Report for the Norwegian Environment Agency 117, 2016.
[16] Weng P, Tang Z, Guo B. Solving magic triangle of tread rubber composites with phosphonium-modified petroleum resin. Polymer 2020;190:122244.
[17] Rodgers B. Tire engineering: an introduction. CRC Press; 2020.
[18] Rodgers B, Tracey D, Waddell W. Tire applications of elastomers; treads. paper h. In: A meeting of the american chemical society rubber division. Grand Rapids, MI; 2004.
[19] Bhattacharyya S, Lodha V, Dasgupta S, Mukhopadhyay R, Guha A, Sarkar P, et al. Influence of highly dispersible silica filler on the physical properties, tearing energy, and abrasion resistance of tire tread compound. J Appl Polym Sci 2019;136(18):47560.
[20] Veiga VD, Rossignol TM, Crespo JdS, Carli LN. Tire tread compounds with reduced rolling resistance and improved wet grip. J Appl Polym Sci 2017;134(39):45334.
[21] Martin PJ, Brown P, Chapman AV, Cook S. Silica-reinforced epoxidized natural rubber tire treads—performance and durability. Rubber Chem Technol 2015;88(3):390–411.
[22] Grosch K. Abrasion of rubber and its relation to tire wear. Rubber Chem Technol 1992;65(1):78–106.
[23] Liang H, Fukahori Y, Thomas A, Busfield J. Rubber abrasion at steady state. Wear 2009;266(1–2):288–96.
[24] Lv X, Wang H, Wang S. Effect of swelling nitrile rubber in cyclohexane on its ageing, friction and wear characteristics. Wear 2015;328:414–21.
[25] Grosch K, Schallamach A. The load dependence of laboratory abrasion and tire wear. Rubber Chem Technol 1970;43(4):701–13.
[26] Nguyen V, Zheng D, Schmerwitz F, Wriggers P. An advanced abrasion model for tire wear. Wear 2018;396:75–85.
[27] Collier B, Warchol J. The effect of inflation pressure on bias, bias-belted and radial tire performance. SAE Trans 1980;552–63.
[28] Li Y, Zuo S, Lei L, Yang X, Wu X. Analysis of impact factors of tire wear. J Vib Control 2012;18(6):833–40.
[29] Wang C, Huang H, Chen X, Liu J. The influence of the contact features on the tire wear in steady-state conditions. Proc Inst Mech Eng Part D: J Automob Eng 2017;231(10):1326–39.
[30] Strigel A, Peckelsen U, Unrau H-J, Gauterin F. Estimation of feasible ranges of functional tire characteristics based on tire dimension, inflation pressure, and wheel load. Proc Inst Mech Eng Part D: J Automob Eng 2019;233(14):3700–6.
[31] Gabor J, Wall J, Rodgers M. Overview of medium radial truck and off the road tire technology. In: Proceedings of the 2001 American chemical society spring meeting, rubber division. Providence, Rhode Island; 2001.
[32] Andersson-Sköld Y, Johannesson M, Gustafsson M, Järlskog I, Lithner D, Polukarova M, et al. Microplastics from tyre and road wear : a literature review. VTI rapport 1028A, Swedish National Road and Transport Research Institute, Environment; 2020, https://urn.kb.se/resolve?urn=urn:nbn:se:vti:diva-15243.
[33] Archard J. Contact and rubbing of flat surfaces. J Appl Phys 1953;24(8):981–8.
[34] Meng H, Ludema K. Wear models and predictive equations: their form and content. Wear 1995;181:443–57.
[35] Podra P, Andersson S. Simulating sliding wear with finite element method. Tribol Int 1999;32(2):71–81.
[36] de Saracibar CA, Chiumenti M. On the numerical modeling of frictional wear phenomena. Comput Methods Appl Mech Engrg 1999;177(3–4):401–26.
[37] Schallamach A, Turner D. The wear of slipping wheels. Wear 1960;3(1):1–25.
[38] Huang H, Chiu Y, Wang C, Jin X. Three-dimensional global pattern prediction for tyre tread wear. Proc Inst Mech Eng Part D: J Automob Eng 2015;229(2):197–213.
[39] Hofstetter K, Grohs C, Eberhardsteiner J, Mang HA. Sliding behaviour of simplified tire tread patterns investigated by means of fem. Comput Struct 2006;84(17–18):1151–63.
[40] Grosch K, Heinz M. Proposal for a general laboratory test procedure to evaluate abrasion resistance and traction performance of tire tread compounds. In: IRC 2000 Rubber Conference. 2000, p. 12–5.
[41] Bürckert M. Realitätsnahe Bewertung des Einflusses der Oberflächenspannung flüssiger Zwischenmedien auf den maximalen Reibschluss zwischen Reifen und Fahrbahn, vol. 70, KIT Scientific Publishing; 2019.
[42] Salehi M, Noordermeer JW, Reuvekamp LA, Dierkes WK, Blume A. Measuring rubber friction using a laboratory abrasion tester (lat100) to predict car tire dry abs braking. Tribol Int 2019;131:191–9.
[43] ISO 23233:2016: Rubber, vulcanized or thermoplastic — Determination of resistance to abrasion using a driven, vertical abrasive disc. Geneva, CH: International Organization for Standardization; 2016, Standard.
[44] ISO 12103-1:2016: Road vehicles — Test contaminants for filter evaluation — Part 1: Arizona test dust. Geneva, CH: International Organization for Standardization; 2016, Standard.
[45] Kakroodi AR, Kazemi Y, Rodrigue D. Mechanical, rheological, morphological and water absorption properties of maleated polyethylene/hemp composites: Effect of ground tire rubber addition. Compos Part B: Eng 2013;51:337–44.
[46] Thomas A, Muniandy K. Absorption and desorption of water in rubbers. Polymer 1987;28(3):408–15.
[47] Zhang M, Unrau H-J, Gießler M, Gauterin F. A detailed tire tread friction model considering dynamic friction states. Tribol Int 2024;193:109342.
[48] Guo K, Lu D. Unitire: unified tire model for vehicle dynamic simulation. Veh Syst Dyn 2007;45(S1):79–99.
[49] Savkoor A. On the friction of rubber. Wear 1965;8(3):222–37.
[50] Shao R, Wahle M, Zimmermann M. A model for the dynamic friction behaviour of rubber-like materials. Tribol Int 2021;164:107220.
[51] Popov VL, Pohrt R. Adhesive wear and particle emission: Numerical approach based on asperity-free formulation of rabinowicz criterion. Friction 2018;6:260–73.
[52] Chen X, Kong Y, Wang M, Huang X, Huang Y, Lv Y, et al. Wear and aging behavior of vulcanized natural rubber nanocomposites under high-speed and high-load sliding wear conditions. Wear 2022;498:204341.
[53] Reitsma M, Cain R, Biggs S, Smith D. Wear of a single asperity using lateral force microscopy. Tribol Lett 2006;24:257–63.
[54] Schallamach A. Recent advances in knowledge of rubber friction and tire wear. Rubber Chem Technol 1968;41(1):209–44.
[55] Persson BN, Tosatti E. Qualitative theory of rubber friction and wear. J Chem Phys 2000;112(4):2021–9.
[56] Schläfle S, Zhang M, Unrau H-J, Gauterin F. Influence of vertical load, inflation pressure, and driving speed on the emission of tire–road particulate matter and its size distribution. Atmosphere 2024;15(4):502.